

Received July 14, 2020, accepted July 25, 2020, date of publication July 28, 2020, date of current version August 13, 2020.

Digital Object Identifier 10.1109/ACCESS.2020.3012533

# Three-Dimensional Localization of a Robotic Capsule Endoscope Using Magnetoquasistatic Field

SI-LIANG LIU<sup>1</sup>, JAYOUNG KIM<sup>2</sup>, BYUNGJEON KANG<sup>1,2</sup>, EUNPYO CHOI<sup>1</sup>,  
AYOUNG HONG<sup>3</sup>, (Member, IEEE), JONG-OH PARK<sup>1</sup>, (Member, IEEE),  
AND CHANG-SEI KIM<sup>1</sup>, (Member, IEEE)

<sup>1</sup>School of Mechanical Engineering, Chonnam National University, Gwangju 61186, South Korea

<sup>2</sup>Korea Institute of Medical Microrobotics, Gwangju 61011, South Korea

<sup>3</sup>Department of Robotics Engineering, Chonnam National University, Gwangju 61186, South Korea

Corresponding authors: Jayoung Kim (jaya@kimiro.re.kr), Jong-Oh Park (jop@jnu.ac.kr), and Chang-Sei Kim (ckim@jnu.ac.kr)

This work was supported by a grant of the Korea Health Technology Development Research and Development Project through the Korea Health Industry Development Institute (KHIDI) funded by the Ministry of Health and Welfare, South Korea, under Grant HI19C0642.

**ABSTRACT** Recent research efforts regarding advanced Robotic Capsule Endoscopes (RCEs) have primarily focused on the development of actively locomotive endoscope capsules. However, accurate movement of an RCE inside the digestive organs remains a challenge that hinders the further development of an autonomous RCE that with applicability in clinical practice. To address this challenge, this study proposed and developed a novel three-dimensional (3D) location positioning method that is compatible with an RCE manipulated by an external magnetic actuation system. The developed localization methodology employed one embedded single-axis receiving coil (Rx) in the RCE and three external transmitting coils (Tx) placed under the clinical bed. The magnetic flux density obtained from the electromotive force at the Rx was applied to the solution of 3D nonlinear Biot–Savart equations and enabled the determination of the position of the Rx in relation to the corresponding magnetoquasistatic field source in the Tx. For implementation, this study developed: (1) an accurate mathematical model and volumetric analysis method for the magnetoquasistatic field by applying equipotential contour and surface mapping, (2) a method to determine the optimal Tx arrangement, and (3) a prototyped device and in-vitro validation of the feasibility of the 3D localization. In the helical trajectory tracking experiment, the device demonstrated an error of  $2.03 \pm 1.14$  mm, and the feasibility in the clinical environment was verified through gastrointestinal phantom experiments. The proposed method will be further evaluated clinically for the retargeting and accurate localization of internal pathologies as well as the closed-loop control of an actively locomotive RCE.

**INDEX TERMS** 3D localization, electromagnetic induction, magnetoquasistatic field, wireless position sensing, robotic capsule endoscope.

## I. INTRODUCTION

The development of an actively locomotive untethered capsule endoscope utilizing an External Magnetic Actuation (EMA) system has been extensively studied in recent years [1]–[5]. As a promising alternative to traditional clinical endoscopy, the untethered capsule endoscope facilitates the active investigation of the entire gastrointestinal (GI) tract

The associate editor coordinating the review of this manuscript and approving it for publication was Aysegül Ucar<sup>1</sup>.

while considerably reducing pain without anesthesia [6]–[9]. However, wireless Robotic Capsule Endoscope (RCE) technology requires further development to overcome several issues, including accurate lesion localization, the navigation of active locomotive RCEs [10], high-efficiency wireless power transmission [11], and other functionalities such as drug delivery performance [12], biopsy [13], and tattooing [14]. These functionalities are critical to the future development of RCEs and depend significantly on having accurate information regarding the RCE position and

orientation. However, sensing the RCE position remains difficult due to the complex geometry inside the GI tract [15] and the wireless environment [16].

Several studies have investigated RCE localization methods, including those based on Radio Frequency (RF) signals, magnetoquasistatic magnetic fields, magnetic sensors, gamma rays, and computer vision technologies. In 2005, Hu *et al.* developed a (two-dimensional) 2D sensor array for estimating the position and orientation of an RCE [17]. Son *et al.* also employed a 2D sensor array with an improved signal processing method [18]. The external Hall effect sensor arrays were used to detect the steady magnetic field generated by a permanent magnet embedded in the RCE. A gamma ray based strategy has also been studied; in 2014, Than *et al.* developed a localization system consisting of three  $^{22}\text{Na}$  markers with a diameter of less than 1 mm embedded in the cover of the RCE, which could be detected by a gamma-ray system [19]. Recently, an image-based strategy has also been studied extensively, in which videos or sequential visual images obtained during diagnostics using an embedded camera are employed for the development of the localization algorithm; Marya *et al.* clinically tested the performance of this method [20] based on video localization were presented in [21]–[24]. In addition, hybrid localization strategies have been discussed, such as video- and RF-based [25] and video- and magnetic-sensor based methods [26].

However, these previously investigated methods have their disadvantages. For example, angiography or gamma ray based methods would expose patients to radiation during the diagnostic process, and video-based localization strategies have issues due to their continuously increasing error and uncertain image quality. Further, RF-based strategies result in signal attenuation and distortion issues owing to the dielectric properties of human tissues [27]–[32]. The primary problem with magnetic sensor-based methods is the requirement for the sensors to be located in an arrayed configuration surrounding the human body to achieve localization and compatibility with an EMA system [33]. Each steady magnetic field for locomotion and positioning could result in undesired interference between the sensing and actuation signals.

In contrast, magnetoquasistatic field based methods (using a low-frequency oscillating steady field of 30 kHz to 300 kHz) showed promising results owing to their compatibility with EMA systems [34]. The magnetoquasistatic field does not affect the movement of an RCE under the control of an EMA system and can be detected through the low-frequency induction of a magnetic dipole or a current loop, allowing its excellent penetrability of human tissue to be leveraged. Several studies have investigated magnetoquasistatic field based localization methods. Plotkin *et al.* presented a localization method incorporating a single-axis Rx embedded inside the capsule to detect the magnetic fields generated by multiple external TxS [35], [36]. In 2014, Islam and Fleming proposed a 6D localization system comprising three orthogonal rectangular RxS and three orthogonal circular TxS based on the magnetic dipole principle [37]. However,

the arrangement of the concentric orthogonal TxS indicated that the region of interest (ROI) in the space diverged outward from the center. This could complicate the application of a concentric orthogonal TxS configuration to a capsule endoscope in a clinical setting because the GI tract is compact and concentrated in a limited space. To develop localization method using an alternating magnetic field, Abbott *et al.* applied a rotating external permanent magnet, with goals of localizing and propelling a spiral-shape capsule through the alternating magnetic field [38].

A magnetoquasistatic-field-based RCE localization method employing a novel coil configuration was introduced in this study to overcome these wireless RCE localization problems. The proposed method utilized a low-frequency magnetic field signal with a greater ability to penetrate the human body. The proposed system was composed of three TxS placed into a clinical bed and a single Rx embedded into a capsule endoscope. A 200 mm diameter sphere represented the ROI containing most of the GI organs, as shown in Fig. 1.

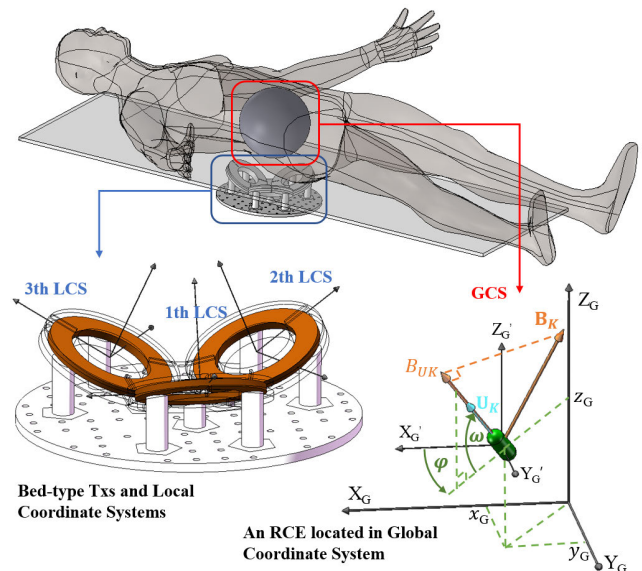


FIGURE 1. A schematic of the proposed RCE localization system.

Compared with [37], this arrangement produced a stronger primary magnetic field that could be concentrated in the ROI and enabled a compact bed-type design that occupied minimal space. Specifically, the low-frequency electromotive force (emf) signals induced by the magnetoquasistatic fields of three TxS were separately transmitted to an Rx embedded in the RCE. The amplitude of the signal received was then transformed into the magnitude of the magnetoquasistatic field, and the three-dimensional (3D) position was computed by solving the magnetic field inverse problem. The orientation of the RCE could be treated as a known parameter by leveraging an EMA that could precisely control the orientation of the RCE and, thus, simplify its localization.

The main contribution of this study is the demonstration of a novel 3D RCE localization method compatible with EMA

by using minimum numbers of Tx and Rx coils utilization, which could be implemented at the clinical bedside. In detail, this study proposed and developed (1) an RCE localization method capable of EMA cooperation, (2) an accurate mathematical model of a magnetoquasistatic field based on the Biot-Savart law, (3) an optimal Tx arrangement for multiple Tx configuration, (4) a complete localization algorithm that provides the conversion of an oscillating voltage to the flux density of a steady magnetic field including coordinate transformation, and (5) a volumetric magnetoquasistatic field analysis method that employs an equipotential surface and a contour map. Moreover, the proposed method was prototyped and verified through in-vitro experiments using X-ray images. These contributions are anticipated to advance the ability to provide 3D localization for RCEs in clinical settings.

The remainder of this paper is organized as follows. Section II introduces the theoretical basis of the proposed method. In Section III, the simulation results and analysis are presented. The experimental setup and results are discussed in Section IV. Finally, concluding remarks with potential directions of future studies are presented in Section V.

## II. 3D LOCALIZATION METHOD

The overall flow chart of the proposed localization method is presented in Fig. 2. In accordance, detail explanations are follows in this section.

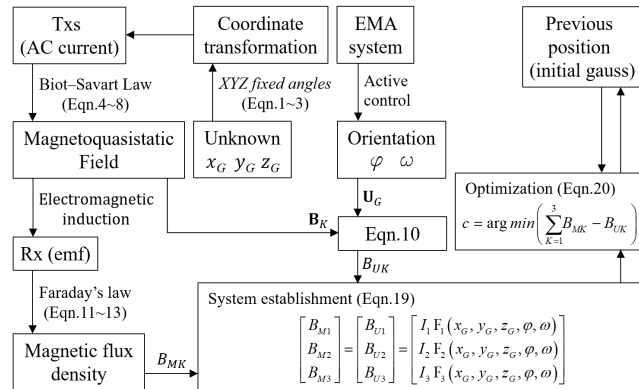


FIGURE 2. An overall block diagram of the proposed RCE localization method.

### A. COORDINATE TRANSFORMATION

As shown in Fig. 1, the local position of the RCE was transformed into global coordinates for registration to a pre-operative image and coordination with the external actuator.  $X_G Y_G Z_G$  is the reference global coordinate system (GCS) placed on a fixed point on the bed and  $X_K Y_K Z_K$  is the local coordinate system (LCS) attached to the K-th Tx. The K-th Tx lies in the x-y plane and is concentric with the origin of the K-th LCS.

First, given the location and orientation of the RCE as  $P_G(x_G, y_G, z_G, \varphi, \omega)$  in the GCS, the spatial relationship

between the GCS and K-th LCS was derived using the *XYZ fixed angles* method [39]. The coordinate was rotated in the GCS about the x, y, and z axes by angles  $\gamma_K$ ,  $\beta_K$ , and  $\alpha_K$ , respectively. The rotation matrix from the K-th LCS to the GCS is then obtained as

$$R_K^G = \begin{bmatrix} c\alpha_K & -s\alpha_K & 0 \\ s\alpha_K & c\alpha_K & 0 \\ 0 & 0 & 1 \end{bmatrix} \begin{bmatrix} c\beta_K & 0 & s\beta_K \\ 0 & 1 & 0 \\ -s\beta_K & 0 & c\beta_K \end{bmatrix} \times \begin{bmatrix} 1 & 0 & 0 \\ 0 & c\gamma_K & -s\gamma_K \\ 0 & s\gamma_K & c\gamma_K \end{bmatrix} \quad (1)$$

where  $c\alpha_K$  is  $\cos(\alpha_K)$ , and  $s\alpha_K$  is  $\sin(\alpha_K)$ . The rotation matrix of the GCS relative to the K-th LCS is defined as  $R_K^G = R_K^{GT}$ . After the rotation, this coordinate is translated along the z-axis by  $t_K$ , and the position of the GCS's origin (GORG) with respect to the K-th LCS,  $\mathbf{P}_{GORG}^K$ , is expressed as  $\mathbf{P}_{GORG}^K = [0 \ 0 \ t_K]^T$ . The position of the K-th LCS's origin (KORG) with respect to the GCS can then be obtained as

$$\mathbf{P}_{KORG}^G = -R_K^G \mathbf{P}_{GORG}^K \quad (2)$$

An arbitrary position  $\mathbf{P}_G[x_G \ y_G \ z_G]^T$  of the RCE with respect to the GCS can be transformed into  $\mathbf{P}_K[x_K \ y_K \ z_K]^T$  in terms of the K-th LCS by using the following transformation.

$$\mathbf{P}_K = R_K^G \mathbf{P}_G + \mathbf{P}_{KORG}^K \quad (3)$$

### B. MAGNETOQUASISTATIC FIELD MODEL

The magnetic flux density  $\mathbf{B}_K$  generated by the K-th Tx at the arbitrary position  $\mathbf{P}_G$  was derived by the Biot-Savart law, as shown in [40].

$$\mathbf{H} = \oint \frac{I d\mathbf{L} \times \mathbf{R}}{4\pi R^3} \quad (4)$$

where  $\mathbf{H}$  is the magnitude of the magnetic field intensity,  $I$  is the current in the differential length of the filament vector  $d\mathbf{L}$ ,  $\mathbf{R}$  is the direction vector along  $d\mathbf{L}$  to an arbitrary point, and  $R$  is the magnitude of the vector  $\mathbf{R}$ . For a circular shaped Tx, the magnetic density properties in (4) are obtained as follows:

$$d\mathbf{L} = r_K d\theta (-s\theta \vec{i}_K + c\theta \vec{j}_K); \quad (5)$$

$$\mathbf{R} = (x_K - r_K c\theta) \vec{i}_K + (y_K - r_K s\theta) \vec{j}_K + z_K \vec{k}_K; \quad (6)$$

$$R = \left[ (x_K - r_K c\theta)^2 + (y_K - r_K s\theta)^2 + (x_K - r_K c\theta)^2 + z_K^2 \right]^{1/2} \quad (7)$$

where  $r_K$  is the radius of the K-th Tx;  $\vec{i}_K$ ,  $\vec{j}_K$ , and  $\vec{k}_K$  are the unit vectors representing the x-, y- and z-axes of the K-th LCS, respectively; and  $\theta$  is the integration variable.

By substituting Equations (5), (6), and (7) into (4), the magnetic field intensity at each Tx can then be computed as (8), as shown at the bottom of the next page, where  $N_K$  is the number of coil turns, and  $I_K$  is the current of the K-th Tx. Further, the magnetic flux density  $\mathbf{B}_K$  at  $\mathbf{P}_G$  is defined by  $\mathbf{B}_K = \mu_0 \mathbf{H}_K$ , where  $\mu_0$  is the permeability of a vacuum.

By using a unit direction vector,  $\mathbf{U}_G$ , in (9) with respect to the K-th LCS, the direction vector in the GCS is transformed into the LCS as  $\mathbf{U}_K = R_G^K \mathbf{U}_G$ , where

$$\mathbf{U}_G = [\omega c \varphi \quad \omega s \varphi \quad s \omega]^T \quad (9)$$

The magnitude of the magnetic flux density  $\mathbf{B}_K$  for a given orientation of the RCE can then be obtained as follows:

$$B_{UK} = \mathbf{B}_K \cdot \mathbf{U}_K \quad (10)$$

The inductive emf is transformed into the magnitude of the magnetic flux density, which can be measured by the Rx. Herein, the principle of electromagnetic induction that the amplitude of the emf is linearly proportional to the amplitude and frequency of the magnetoquasistatic field is adopted. The emf is given by Faraday's Law as

$$\varepsilon = -N_r \frac{d\phi(V)}{dt} \quad (11)$$

where  $N_r$  is the number of coil turns of the Rx, and  $\phi$  is the magnitude of the magnetic flux through the cross-section of the Rx. As shown in Fig. 3, for a given sinusoidal oscillation,  $\phi$ , the emf should be an oscillating sinusoidal signal with the same period and a phase difference of  $T/4$ , as compared to  $\phi$ . By integrating (11), we obtain the following:

$$\int_0^{T/4} \varepsilon dt = -N_r \int_0^{T/4} d\phi \quad (12)$$

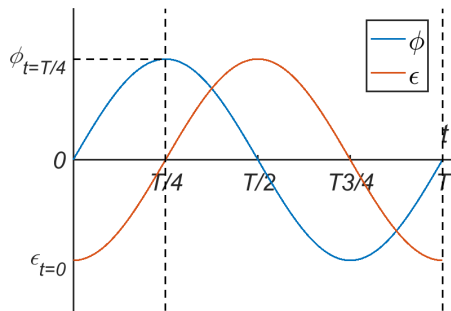


FIGURE 3. Phase relationship with an emf for a given sinusoidal input.

and (12) can be rewritten as (13) for computational analysis as follows:

$$\varepsilon_{t=0} \left( \frac{T}{4} - 0 \right) = -N_r (\phi_{t=T/4} - \phi_{t=0}) \quad (13)$$

Because  $\phi_{t=0} = 0$ ,  $\phi_{t=T/4} = -\varepsilon_{t=0} / (4fN_r)$ , where the terms  $\phi_{t=T/4}$  and  $-\varepsilon_{t=0}$  can be considered as the absolute peak values of  $\phi$  and  $\varepsilon$ , respectively. Thus, rewriting  $\phi_{t=T/4}$  and  $\varepsilon_{t=0}$  as  $\phi_{peak}$  and  $\varepsilon_{peak}$ , respectively,  $\phi_{peak} = \varepsilon_{peak} / (4fN_r)$  is obtained. Finally, the measured magnetic flux density  $B_{MK}$  for the RCE with respect to the K-th Tx can

be expressed as  $B_{MK} = \phi_{peak} / A_r$ , where  $A_r = \pi D_r^2 / 4$  is the cross-sectional area of the Rx, and  $D_r$  is the diameter of the Rx.

### C. POSITION COMPUTATION

Three Tx's are triggered in sequence to provide three independent equations for solution to determine the three unknown parameters,  $x_G$ ,  $y_G$ , and  $z_G$ . The proof of this approach is given in this section.

As stated in (8), the components of the magnetic flux density along the three axes are all functions of the unknowns  $x_G$ ,  $y_G$ , and  $z_G$ . Thus, magnetic flux densities of Tx1, Tx2, and Tx3 under 1A of current at an arbitrary position  $\mathbf{P}_G [x_G \ y_G \ z_G]^T$  can be expressed as

$$\begin{aligned} \mathbf{B}_{1\_1A} &= \begin{bmatrix} b_{1i}(x_G, y_G, z_G) \\ b_{1j}(x_G, y_G, z_G) \\ b_{1k}(x_G, y_G, z_G) \end{bmatrix}, \\ \mathbf{B}_{2\_1A} &= \begin{bmatrix} b_{2i}(x_G, y_G, z_G) \\ b_{2j}(x_G, y_G, z_G) \\ b_{2k}(x_G, y_G, z_G) \end{bmatrix}, \quad \text{and} \\ \mathbf{B}_{3\_1A} &= \begin{bmatrix} b_{3i}(x_G, y_G, z_G) \\ b_{3j}(x_G, y_G, z_G) \\ b_{3k}(x_G, y_G, z_G) \end{bmatrix}. \end{aligned} \quad (14)$$

The flux density of the magnetic field established by an arbitrary position with respect to a fixed structure Tx is proportional only to the magnitude of the current input to each coil. Thus, the established magnetic flux density in the presence of  $I_1$ ,  $I_2$  and  $I_3$ , which are the currents input to Tx1, Tx2, and Tx3, respectively, is given by

$$\begin{aligned} \mathbf{B}_{123} &= I_1 \mathbf{B}_{1\_1A} + I_2 \mathbf{B}_{2\_1A} + I_3 \mathbf{B}_{3\_1A} \\ &= \begin{bmatrix} I_1 b_{1i} + I_2 b_{2i} + I_3 b_{3i} \\ I_1 b_{1j} + I_2 b_{2j} + I_3 b_{3j} \\ I_1 b_{1k} + I_2 b_{2k} + I_3 b_{3k} \end{bmatrix} \end{aligned} \quad (15)$$

The net magnetic field magnitude along with the direction of the RCE is then obtained as

$$B_{nm} = \mathbf{B}_{123} \cdot \mathbf{U}_G = \begin{bmatrix} I_1 b_{1i} + I_2 b_{2i} + I_3 b_{3i} \\ I_1 b_{1j} + I_2 b_{2j} + I_3 b_{3j} \\ I_1 b_{1k} + I_2 b_{2k} + I_3 b_{3k} \end{bmatrix} \cdot \begin{bmatrix} \omega c \varphi \\ \omega s \varphi \\ s \omega \end{bmatrix} \quad (16)$$

The expansion of (16) yields:

$$B_{nm} = [I_1 \quad I_2 \quad I_3] \begin{bmatrix} F_1 \\ F_2 \\ F_3 \end{bmatrix} \quad (17)$$

$$\mathbf{H}_K = \frac{N_K I_K r_K}{4\pi} \int_0^{2\pi} \frac{z_K c \theta \vec{i}_K + z_K s \theta \vec{j}_K + (-x_K c \theta - y_K s \theta + r_K) \vec{k}_K}{[x_K^2 + y_K^2 + z_K^2 + r_K^2 - 2r_K(x_K c \theta + y_K s \theta)]^{1.5}} d\theta \quad (8)$$

where

$$\begin{cases} F_1(x_G, y_G, z_G, \varphi, \omega) = b_{1i}c\omega c\varphi + b_{1j}c\omega s\varphi + b_{1k}s\omega \\ F_2(x_G, y_G, z_G, \varphi, \omega) = b_{2i}c\omega c\varphi + b_{2j}c\omega s\varphi + b_{2k}s\omega \\ F_3(x_G, y_G, z_G, \varphi, \omega) = b_{3i}c\omega c\varphi + b_{3j}c\omega s\varphi + b_{3k}s\omega \end{cases}$$

The matrix  $B_{nm}$  in (17) has a rank 3 where three independent nonlinear functions,  $F_1$ ,  $F_2$ , and  $F_3$ , are given by Tx1, Tx2, and Tx3, respectively. The lack of any one of these TxS reduces the rank of the matrix to be 2, such that three unknown parameters cannot be identified mathematically. Furthermore, the simultaneous presence of  $I_1$ ,  $I_2$  and  $I_3$  will create magnetic fields with various structures, which lead to the more complex nonlinear system, resulting in computational difficulties. Hence, to decrease the computational burden, the optimal magnetic field in terms of the most concise nonlinear system would be obtained by triggering three TxS sequentially as follows:

$$\begin{aligned} B_{U1} &= \begin{bmatrix} I_1 & 0 & 0 \end{bmatrix} \begin{bmatrix} F_1 \\ F_2 \\ F_3 \end{bmatrix} = I_1 F_1(x_G, y_G, z_G, \varphi, \omega) \\ B_{U2} &= \begin{bmatrix} 0 & I_2 & 0 \end{bmatrix} \begin{bmatrix} F_1 \\ F_2 \\ F_3 \end{bmatrix} = I_2 F_2(x_G, y_G, z_G, \varphi, \omega) \\ B_{U3} &= \begin{bmatrix} 0 & 0 & I_3 \end{bmatrix} \begin{bmatrix} F_1 \\ F_2 \\ F_3 \end{bmatrix} = I_3 F_3(x_G, y_G, z_G, \varphi, \omega) \end{aligned} \quad (18)$$

Combined with the measured magnetic flux density, the three unknown parameters,  $x_G$ ,  $y_G$ , and  $z_G$  can be determined for the three given independent equations of the three magnetic fields generated by the three TxS as follows:

$$\begin{bmatrix} B_{M1} \\ B_{M2} \\ B_{M3} \end{bmatrix} = \begin{bmatrix} B_{U1} \\ B_{U2} \\ B_{U3} \end{bmatrix} = \begin{bmatrix} I_1 F_1(x_G, y_G, z_G, \varphi, \omega) \\ I_2 F_2(x_G, y_G, z_G, \varphi, \omega) \\ I_3 F_3(x_G, y_G, z_G, \varphi, \omega) \end{bmatrix} \quad (19)$$

However, because (19) is a highly nonlinear equation, a numerical solution is not easily obtained manually. In this study, the nonlinear solver, *lsqnonlin*, using the optimization algorithm *trust-region-reflective*, was applied to solve the high-order nonlinear equation in (19). The cost function is defined as

$$c = \arg \min \left( \sum_{K=1}^3 B_{MK} - B_{UK} \right) \quad (20)$$

Equation (20) provides the optimal solution of  $x_G$ ,  $y_G$ , and  $z_G$  by minimizing the error between the measured magnetic field and the model values.

### III. CONFIGURATION AND ROI ANALYSIS

This section presents the optimal arrangement of the TxS and the physical concept of the proposed localization method.

The conceptual equipotential surfaces and contour maps of the three magnetoquasistatic fields were established for the three TxS, and the appropriate height of the spherical ROI was then determined based on the simulations and analysis.

#### A. TRANSMIT COIL CONFIGURATION

Arrangement of the three TxS in a manner that provides the most effective localization performance is crucial to practical application. Because TxS are required to face the ROI to maximize the magnetic field reception by the Rx, the optimal spatial relationships among the three TxS need to be determined to obtain the best Tx configuration, which relates to the symmetrical properties of the three TxS and the average error of the localization. Therefore, a new measure, termed the *degree of symmetry (DOS)*, is introduced and defined to express the symmetrical properties among the TxS as follows:

$$DOS = \frac{1}{\sqrt{\frac{1}{3} \sum_{i=1}^3 (\text{angle}_i - \overline{\text{angle}})^2}} \quad (21)$$

where  $\text{angle}_i$  and  $\overline{\text{angle}}$  are the angles between the centers of each Tx and the average of these three angles, respectively. The z-axis of the K-th LCS indicates the center of the K-th Tx. Because the *DOS* is computed using the reciprocal of the standard deviation of each angle, a higher *DOS* represents a more symmetrical arrangement of the transmittance coils configuration.

A brute-force searching simulation was performed as follows to determine the Tx configuration. First,  $\beta_K$  was fixed at  $0^\circ$ , wherein all the TxS were directed toward the center of the ROI, and  $t_K$  was fixed at 0.15 m, wherein all the TxS were placed at the same distance from the ROI. Then,  $\gamma_K$  and  $\alpha_K$  were considered as variables to simulate all possible Tx arrangements in 3D space.  $\gamma_K$  and  $\alpha_K$  were randomly selected from the interval of  $-180^\circ \sim 180^\circ$ , and a total of 8000 cases comprising various TxS arrangements were prepared for the examination. Second, 32 positions that were uniformly distributed in the ROI were chosen, and 18 orientations were selected for each position such that a total of 594 combinations of RCE position and orientation were obtained for use as ground truth positions. Third, the ideal flux density  $B_{UK}$  was computed using Equations (1)–(10), and the measurement flux density  $B_{MK}$  was simulated by adding random noise at a level of 1–5% of the full range of  $B_{UK}$  at each ground truth location. Fourth, position estimation was performed using the proposed localization method. Finally, the average errors for all possible Tx arrangements were calculated. Fig. 4 provides the simulation results, which verified that the Tx arrangements with lower localization error tended to have higher *DOS*s, which indicated greater Tx symmetry. The simulation result provided the Tx configuration having the highest *DOS*, which satisfied both the symmetry condition and the requirements for the design of a bed-type system.

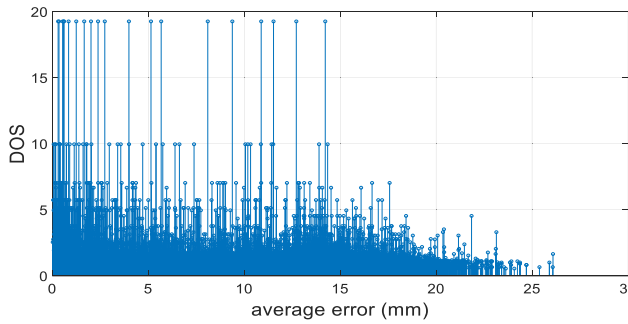


**FIGURE 4.** The relationship between average error and DOS. Higher DOS of arrangement case lead to smaller error of estimation.

### B. EQUIPOTENTIAL SURFACE AND CONTOUR MAP

The proposed localization method was analyzed based on equipotential surfaces and contour maps. In the proposed method, three magnetic flux densities,  $B_{M1}$ ,  $B_{M2}$ , and  $B_{M3}$ , from each Tx coil were measured by activating each coil sequentially to determine the three unknown parameters  $x_G$ ,  $y_G$ , and  $z_G$ . For each Tx, an equipotential surface exists such that the flux density is equal to  $B_{MK}$  at any position on that surface. The location of the RCE should be detected at the intersection of these three equipotential surfaces. For illustration purposes, an example position  $P_G(0, 0, 0, 0^\circ, 90^\circ)$  was used, which represented that the RCE was located at the origin, and its orientation was along the z-axis of the GCS.

The brown, gray, and green regions in Fig. 5(a) are the equipotential surfaces of the first, second, and third Tx, respectively. The simulation procedure was as follows: (i) the flux density at the selected positions, which were uniformly distributed in 3D space, were computed using the mathematical model developed in this study; (ii) the flux density in the orientation of the RCE was computed using equation (10) at the selected positions; (iii) the equipotential surface was plotted using the *isosurface* function using the data in the second step.

In this study, the equipotential surface potentials were obtained from the magnitude of the magnetic flux density in the orientation of the RCE. Therefore, the position and shape of the equipotential surface depended on both the position and orientation of the RCE. As shown in Fig. 5(a), the three equipotential surfaces intersected each other, forming two intersection points, indicated by the blue and red points in the figure. The blue point was located at  $[0\ 0\ 0]^T$ , which is the exact desired solution, and the red point was located at  $[0\ 0\ -0.108]^T$ , which was a secondary solution of the model. Although the RCE orientation would change the posture of the equipotential surface, the secondary solution always formed at the lower region having certain distances from the desired solution. This distribution indicated that the velocity constraint could be applied based on the distance interval between the desired and secondary solutions. Accordingly, an algorithm was applied to select an appropriate ROI, and a near-position finding constraint based on the RCE velocity was utilized such that the secondary solutions could be eliminated.

The magnetoquasistatic field contour map of the three Tx was employed for predicting the spatial distribution of all possible solutions; a reasonable ROI could be designated based on the analysis of this contour map. Fig. 5(b) shows the contour map of the first and second Tx for the example position  $P_G(0, 0, 0, 0^\circ, 90^\circ)$ . The contour of the third Tx completely coincided with that of the second Tx, because they are symmetric about the y-z plane. The red point represents the secondary solution, which was located at  $[0\ 0\ -0.108]^T$ . Fig. 5(c) presents a contour map consisting of multiple magnetic field levels. The dotted line indicates the  $z = -0.08\ m$  level that separates the secondary solutions from the desired solutions. All intersections above the dotted line are desired solution sets, and all secondary solutions are located in the region of  $z < -0.08\ m$  and are concentrated near  $y = 0\ m$ . Furthermore, the region above  $-0.08\ m$  is the unique solution region and sufficient to be considered the ROI, once the RCE is restricted in the y-z plane and its orientation is aligned with  $\varphi = 0^\circ$  and  $\omega = 90^\circ$ . The contour maps for the various planes should be investigated to provide comprehensive knowledge of the 3D spatial distribution of the secondary solutions.

### C. ROI DETERMINATION

The appropriate ROI can be determined based on the proposed criterion that the secondary solution is always below the desired solution.

A simulation was performed to identify the effects of the secondary solution on the localization ability in ROIs at different heights (i.e., z-axis values). The simulation was performed as follows: (i) 14 spherical ROIs located on the GCS z-axis at an interval of 0.01 m between  $-0.03\ m$  and  $0.1\ m$  were selected as candidates, and a total of 150 000 combinations of positions and orientations were selected as the ground truth values for each ROI candidate; (ii) the magnetic flux density,  $B_{UK}$ , was computed using Equations (1)–(10), and  $B_{MK}$  was computed by adding random noise at a level of 1–5% of the full range of  $B_{UK}$  at each ground truth for every ROI candidate; (iii) the 3D position for each ROI candidate was estimated via the proposed localization method. The simulation result shows that the average error decreases from 3.78 mm to 0.34 mm as the height of the ROI increased from  $z = -0.03\ m$  to  $z = 0.1\ m$ . However, a higher ROI could not only prevent the computation from obtaining secondary solutions but could also cause the signals to suffer due to the low SNR. A low SNR results in poor estimation accuracy, which could be observed from  $z = 0.08\ m$  to  $z = 0.1\ m$ . Based on the simulation results, a 200 mm sphere located at  $[0\ 0\ 0.05]^T$  was selected as the ROI because the magnetic field was not over-attenuated at this location.

## IV. EXPERIMENTAL RESULTS

### A. EXPERIMENTAL SETUP

The experimental setup is shown in Fig. 6(a) and in detail instrumentations are provided in Table 1. An Rx-embedded RCE was fixed at the end effector of an articulated robotic

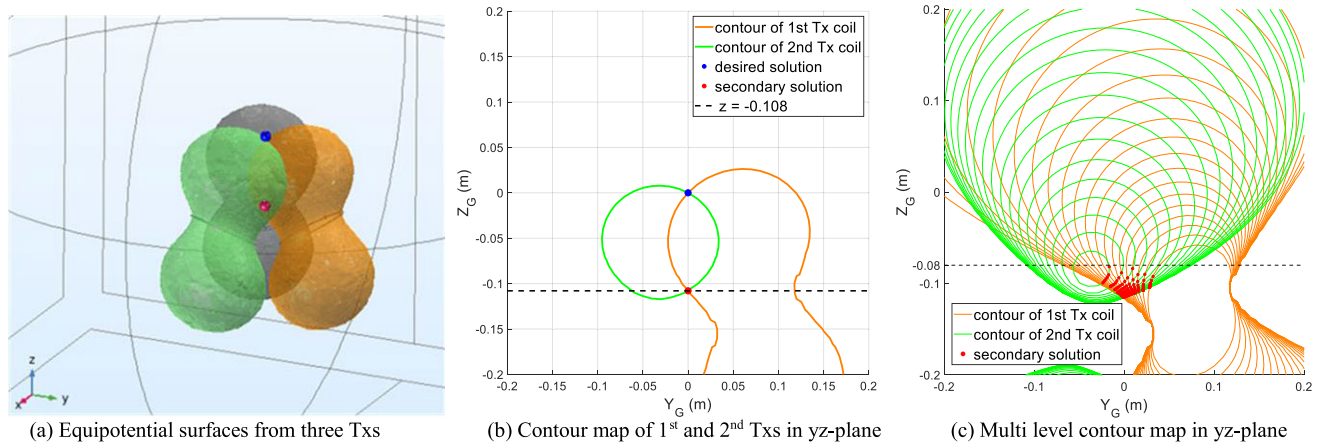


**FIGURE 5.** Equipotential surface and contour map analysis to visualize the magnetoquasistatic field from three Tx coils and find a position of the RCE comes from the intersection of the formed field in each Tx coil.

arm. The Tx coils were located below the RCE and generated the magnetoquasistatic field. A gel block mimicking human tissue was placed between the Rx and Tx coils to evaluate the magnetic distortions that occur through different mediums. A current transformer monitored the AC current in real-time to compensate for current changes due to external disturbances, such as thermal effects. A data acquisition (DAQ) board was incorporated to measure the inductive emf from the Rx and the signal from the current transformer. The switching functions were performed by three pairs of relays and optocouplers that closed and opened the relative loop of the Tx sequentially according to the digital signal from the DAQ, the order of which was controlled by a customized LabVIEW program. A function generator and amplifier supplied AC power for the Tx coils, and capacitors were used to build the resonance for the Tx coils.

Fig. 6(b) shows the design procedure for the controller, which consisted of the following: (i) one Tx coil was activated, and the inductive emf from the Rx and the oscillating voltage signal from the current transformer were measured simultaneously, which was repeated for each Tx; (ii) the emf and the transformer signal were used to determine the flux density and the amplitude of the corresponding AC current; (iii) 3D position was calculated by the proposed localization method for each cycle.

### B. HELICAL TRAJECTORY TRACKING

An experiment was performed to evaluate the reliability and accuracy of the proposed localization method. In the experiment, the RCE moved along the 3D helical trajectory with various orientations. The orientation angle  $\omega$  was fixed at  $45^\circ$ , and  $\varphi$  was rotated sequentially. During the RCE movement, the 3D position computation was performed 1000 times using the developed system.

The reconstructed path is presented in Fig. 7, where the yellow circles at the bottom are the Tx coils, the grey shaded area is the ROI of the system, the blue helical curve is the

**TABLE 1.** Summary of Instrumentation in Experiments.

Instrument	Specification	
	Rx	Tx
number of turns	300	240
copper wire diameter	0.08 mm	0.8 mm
length	10 mm	6.5 mm
outer/inner diameter	10 mm / 5 mm	114 mm / 74 mm
Robotic Arm	LBR iiwa 7 R800	
Function Generator	Agilent 33220A	
Amplifier	HSA 4101	
DAQ	NI USB-6351	
Current Transformer	CST2010-080LB	
Relays	K1AL012W-LB	
Optocouplers	PC817	
Film Capacitors	KEMET R76 Series	
Coil Frame Material	VeroClear	
AC Current Frequency	50 kHz	

desired path, and the red helical path is the estimated path. The total average error, minimum error, maximum error, and the average sampling rate were  $2.03 \pm 1.14$  mm, 0.44 mm, 5.13 mm, and 5 Hz, respectively. The results obtained demonstrated that the developed localization system reconstructed the actual dynamic path of the RCE accurately in the presence of the human-like gel block. The raw data obtained in the experiment is presented in Fig. 8.

Table 2 summarizes the comparison of the proposed method with other technologies available. Where the key performance measures used are the root-mean-square error (RMSE) [mm] for the localization accuracy, working volume [mm  $\times$  mm  $\times$  mm] for the ROI comparison, and sampling rate [Hz] for the circulation time. In Table 2, we could see that the positional accuracy obtained using the proposed method was higher than those based on computer vision or RF signals. The positional accuracy obtained in this study

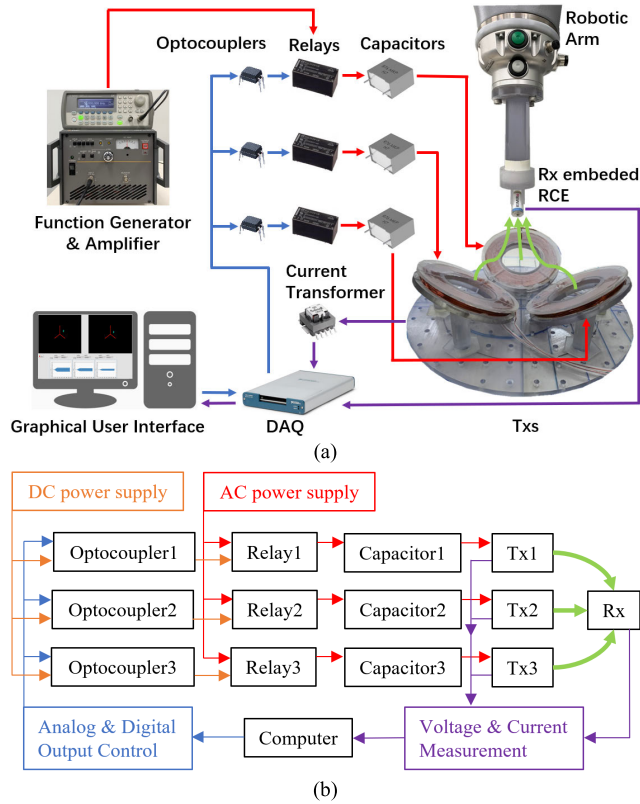


**FIGURE 6.** (a) Experimental setup for helix trajectory tracking test. (b) The circuit block diagram of the controller; AC power supply (Red line), Tx energization sequence control (blue line), signal transformed from Tx to Rx (green line), and signal measurement (purple line).

was similar to that of the magnetic-sensor-based strategy. For the same configuration of the open-type arrangement, a much higher effective distance (200 mm) was obtained than for a magnetic-sensor-based strategy (50 mm). The magnetic moment of the current loop employed in the experiment ( $4.71 \text{ A} \cdot \text{m}^2$ ) as the magnetic source for localization purposes was more than ten times stronger than the largest permanent magnet that can be accommodated in a swallowable endoscope ( $0.45 \text{ A} \cdot \text{m}^2$ , as reported in [15]). These results show that the proposed solution effectively resolved the issues of short effective distance and low SNR. However, the experiments also showed that the proposed solution had a lower update rate (5 Hz) compared to a magnetic-sensor-based strategy (200 Hz).

### C. PHANTOM MODEL EXPERIMENTS

An experiment was conducted in a GI phantom to verify the feasibility of the proposed localization method. A phantom of a human stomach and small intestine was placed above the Tx. An external permanent magnet that was linked to the end effector of the robotic arm was used to induce the RCE to move through the phantom along the designated path and orientation. The movement occurred owing to the force resulting from the interaction between the external and internal permanent magnets embedded in the RCE. Experiments were conducted separately in the stomach and small intestine.

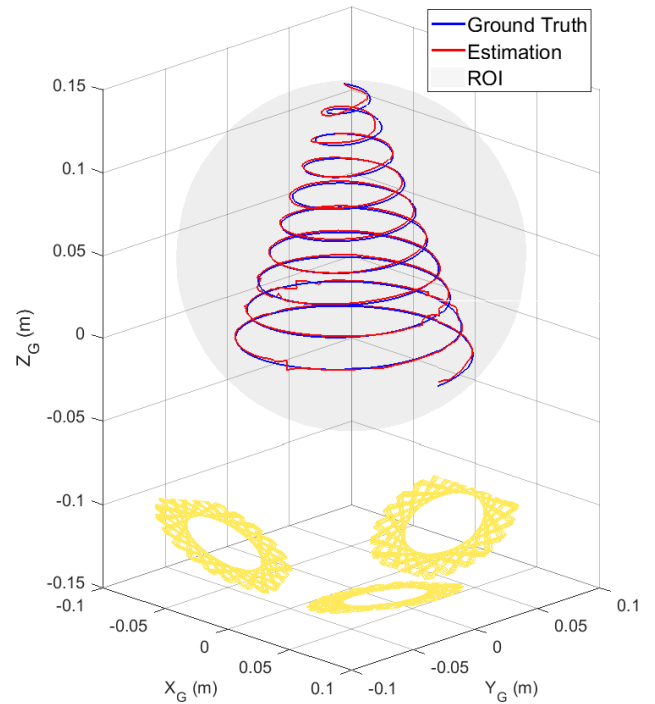


**FIGURE 7.** Experimental result of a 3-dimensional helix trajectory tracking.

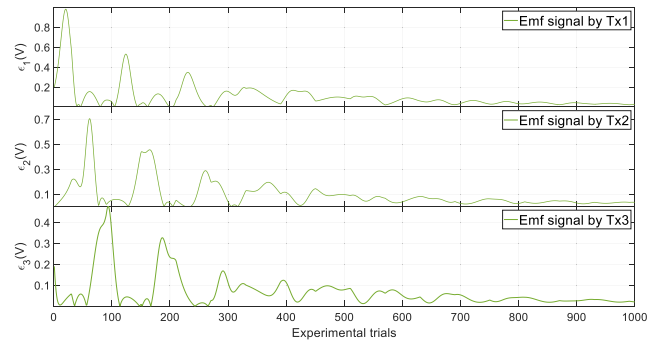


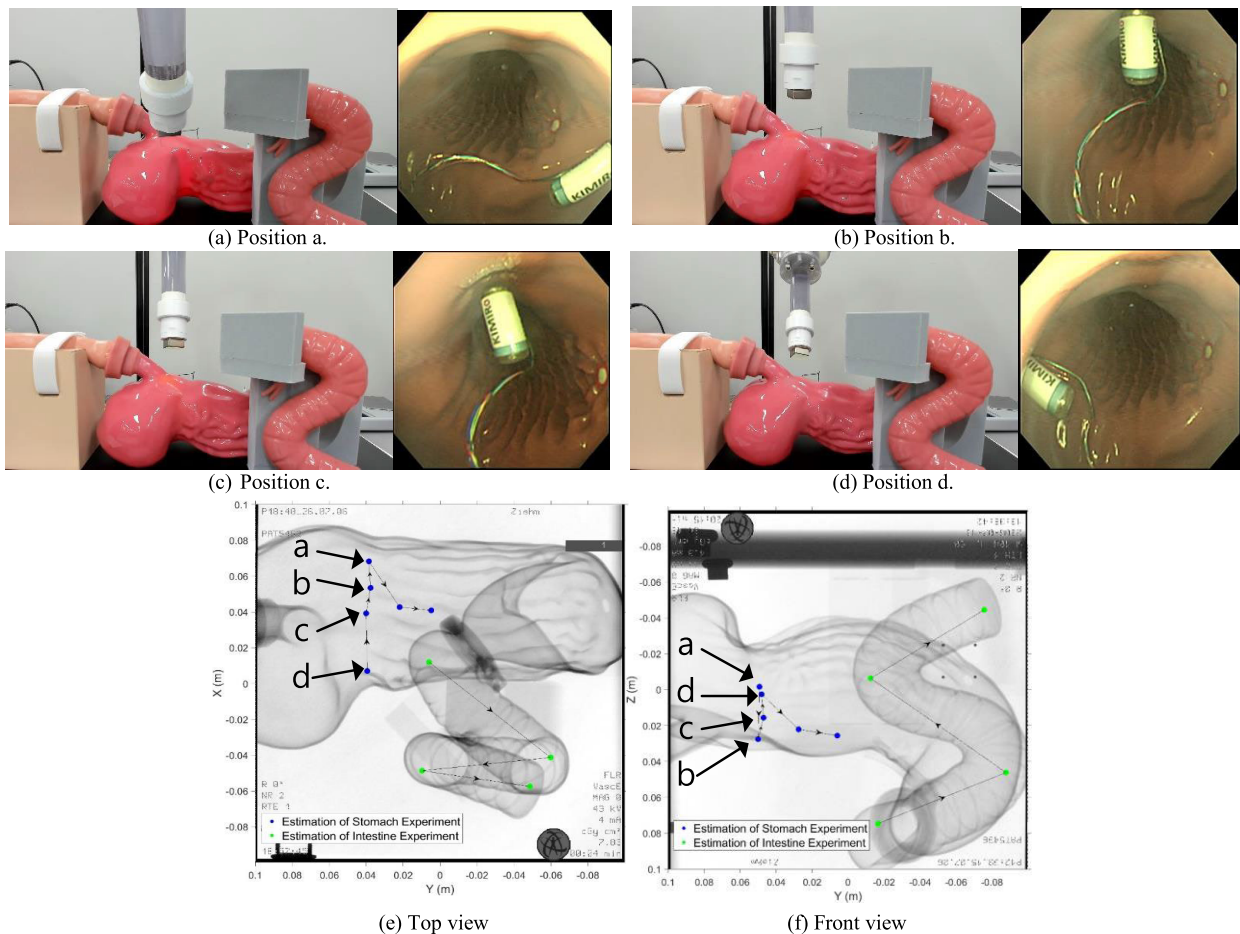
**FIGURE 8.** The measured emf signal in tracking control experiments.

A photograph of the stomach experiment is presented in Fig. 9 (a)–(d). The RCE was actuated by the robotic arm to travel to six positions designated along the lesser curvature. In the first four positions, both the end effector outside the stomach and the RCE inside the stomach were captured, and the latter was captured using a clinical endoscope. Similarly, for the experiment in the small intestine, the RCE reached four designated positions in sequence through the actuation control of the robotic arm.

A photograph of the RCE inside the small intestine could not be captured because of the length limitation of the clinical endoscope. The path for the stomach and small intestine was estimated using the proposed localization method and then overlapped with X-ray images of the phantom in the x-y and y-x planes. The path reconstruction and overlapping results are presented in Fig. 9(e) and (f), which verify that the estimated path matched well with the X-ray images of the stomach and small intestine in the x-y and y-z planes.

**TABLE 2.** Comparison of the Proposed Approach with Other Solutions.

References	Clinical applications in literature				Commercialized industrial device		
	Son et al. [16]	Bao et al. [21]	Pourhomayoun et al. [25]	Plotkin et al. [33]	Proposed method	NDI Wave	Polhemus Fastrack
Strategy	magnetic sensor	computer vision	RF signal	magneto-quasistatic Field	magneto-quasistatic Field	electromagnetic tracking	electromagnetic tracking
Application	capsule endoscope	capsule endoscope	capsule endoscope	general	capsule endoscope	general	general
Number of Transmitters	N/A	N/A	N/A	64	3	N/A	N/A
Working Volume	70×70×50mm <sup>3</sup>	N/A	N/A	288×288×200mm <sup>3</sup>	Spherical in diameter of 200 mm	500×500×500mm <sup>3</sup>	N/A
Sampling Rate	200Hz	2Hz	0.1Hz (16 sensors) 0.33Hz (4 sensors)	50Hz	5Hz	100Hz	120Hz
Position Error	2.1±0.8mm	24.9mm	8.8mm	~1mm	2.03±1.14mm	1.5mm (dynamic) 0.6mm (static)	0.76mm

**FIGURE 9.** The RCE was actuating by the robot arm to travel to four designed position in the phantom model. The reconstruction by the developed localization system and the x-ray image overlap in xy-plane and yz-plane for validation. From a to d position is registered onto a phantom model image captured by an X-ray device.

## V. CONCLUSION

This study proposed a magnetoquasistatic-field-based system for RCE localization consisting of three Tx's under a clinical bed and a single receiving coil inside a capsule body. The developed real-time localization system could provide

accurate 3D positional values for the magnetically manipulated RCE, with the orientation being precisely controlled using the EMA. A magnetic field equipotential surface and contour map analysis was developed to design the Tx configuration and analyze the ability to localize to a specific ROI.

The performance of the designed system was verified through a helical trajectory tracking experiment in open space and an in-vitro phantom model experiment.

The advantages of the proposed magnetoquasistatic field based localization methodology include (i) it could transmit the electromagnetic signal through a human body with negligible attenuation and distortion as compared to an RF-signal-based strategy, and (ii) it could collaborate with a steady magnetic field based EMA system simultaneously and (iii) cover a larger ROI as compared to a magnetic sensor based strategy with minimum number of transmit coils or transducers.

In future work, the proposed localization method will be improved and refined in several aspects. First, the RCE in this study will be developed as a wireless system, which will be accomplished using a commercial analog-to-digital converter (ADC) chip and a Bluetooth chip integrated into the RCE. Second, the penetration performance and robustness to signal distortion of the alternating magnetic field through tissue-like materials should be evaluated in an in vivo environment. Third, although the EMA system facilitates the precise control of the RCE, the GI environment could prevent the RCE from exact alignment with the desired orientation, which could result in an error in clinical application. Therefore, a higher-dimensional localization method that simultaneously considers position and orientation, as well as an advanced control method for the precise robotic actuators and the thermal effects on the coil system, will be developed in future studies.

## REFERENCES

- [1] A. W. Mahoney and J. J. Abbott, "Five-degree-of-freedom manipulation of an untethered magnetic device in fluid using a single permanent magnet with application in stomach capsule endoscopy," *Int. J. Robot. Res.*, vol. 35, nos. 1–3, pp. 129–147, Jan. 2016, doi: [10.1177/0278364914558006](https://doi.org/10.1177/0278364914558006).
- [2] M. C. Hoang, "Independent electromagnetic field control for practical approach to actively locomotive wireless capsule endoscope," *IEEE Trans. Syst. Man, Cybern. Syst.*, early access, Jun. 12, 2019. [Online]. Available: <https://ieeexplore.ieee.org/abstract/document/8736025>, doi: [10.1109/TSMC.2019.2917298](https://doi.org/10.1109/TSMC.2019.2917298).
- [3] Z. Ding, "Gastroenterologist-level identification of small-bowel diseases and normal variants by capsule endoscopy using a deep-learning model," *Gastroenterology*, vol. 157, no. 4, pp. 1044–1054, 2019, doi: [10.1053/j.gastro.2019.06.025](https://doi.org/10.1053/j.gastro.2019.06.025).
- [4] J. Yao, Z. Jiao, and D. Ma, "Adaptive robust control of DC motors with extended state observer," *IEEE Trans. Ind. Electron.*, vol. 61, no. 7, pp. 3630–3637, Jul. 2014, doi: [10.1109/TIE.2013.2281165](https://doi.org/10.1109/TIE.2013.2281165).
- [5] J. Pan, W. Li, and H. Zhang, "Control algorithms of magnetic suspension systems based on the improved double exponential reaching law of sliding mode control," *Int. J. Control, Autom. Syst.*, vol. 16, no. 6, pp. 2878–2887, Dec. 2018, doi: [10.1007/s12555-017-0616-y](https://doi.org/10.1007/s12555-017-0616-y).
- [6] M. C. Hoang, V. H. Le, J. Kim, E. Choi, B. Kang, C.-S. Kim, and J.-O. Park, "Development of an external electromagnetic actuation system to enable unrestrained maneuverability for an endoscopic capsule," in *Proc. IEEE Int. Conf. Cyborg Bionic Syst. (CBS)*, Oct. 2018, pp. 255–260, doi: [10.1109/CBS.2018.8612254](https://doi.org/10.1109/CBS.2018.8612254).
- [7] M. C. Hoang, V. H. Le, J. Kim, E. Choi, B. Kang, J.-O. Park, and C.-S. Kim, "Untethered robotic motion and rotating blade mechanism for actively locomotive biopsy capsule endoscope," *IEEE Access*, vol. 7, pp. 93364–93374, 2019, doi: [10.1109/ACCESS.2019.2927894](https://doi.org/10.1109/ACCESS.2019.2927894).
- [8] Q. Zhang, S. Song, P. He, H. Li, H.-Y. Mi, W. Wei, Z. Li, X. Xiong, and Y. Li, "Motion control of magnetic microrobot using uniform magnetic field," *IEEE Access*, vol. 8, pp. 71083–71092, 2020, doi: [10.1109/access.2020.2986089](https://doi.org/10.1109/access.2020.2986089).
- [9] P. Liu, H. Yu, and S. Cang, "Trajectory synthesis and optimization of an underactuated microrobotic system with dynamic constraints and couplings," *Int. J. Control, Autom. Syst.*, vol. 16, no. 5, pp. 2373–2383, Oct. 2018, doi: [10.1007/s12555-017-0192-7](https://doi.org/10.1007/s12555-017-0192-7).
- [10] J. Kim, P. B. Nguyen, B. Kang, E. Choi, J.-O. Park, and C.-S. Kim, "A novel tip-positioning control of a magnetically steerable guidewire in sharply curved blood vessel for percutaneous coronary intervention," *Int. J. Control, Autom. Syst.*, vol. 17, no. 8, pp. 2069–2082, Aug. 2019, doi: [10.1007/s12555-018-0116-8](https://doi.org/10.1007/s12555-018-0116-8).
- [11] H. Liu, "Flexible power control for wireless power transmission system with infixed Receiver position," *IEEE Access*, vol. 7, pp. 181767–181777, 2019, doi: [10.1109/ACCESS.2019.2902411](https://doi.org/10.1109/ACCESS.2019.2902411).
- [12] K. T. Nguyen, M. C. Hoang, E. Choi, B. Kang, J.-O. Park, and C.-S. Kim, "Medical microrobot—A drug delivery capsule endoscope with active locomotion and drug release mechanism: Proof of concept," *Int. J. Control, Autom. Syst.*, vol. 18, no. 1, pp. 65–75, Jan. 2020, doi: [10.1007/s12555-019-0240-0](https://doi.org/10.1007/s12555-019-0240-0).
- [13] M. Sitti, H. Ceylan, W. Hu, J. Giltinan, M. Turan, S. Yim, and E. Diller, "Biomedical applications of untethered mobile milli/microrobots," *Proc. IEEE*, vol. 103, no. 2, pp. 205–224, Feb. 2015, doi: [10.1109/JPROC.2014.2385105](https://doi.org/10.1109/JPROC.2014.2385105).
- [14] M. C. Hoang, "A wireless tattooing capsule endoscope using external electromagnetic actuation and chemical reaction pressure," *PLoS ONE*, vol. 14, no. 7, pp. 1–17, 2019, doi: [10.1371/journal.pone.0219740](https://doi.org/10.1371/journal.pone.0219740).
- [15] S. Yim and M. Sitti, "3-D localization method for a magnetically actuated soft capsule endoscope and its applications," *IEEE Trans. Robot.*, vol. 29, no. 5, pp. 1139–1151, Oct. 2013, doi: [10.1109/TRO.2013.2266754](https://doi.org/10.1109/TRO.2013.2266754).
- [16] K. Yu, G. Fang, and E. Dutkiewicz, "Position and orientation accuracy analysis for wireless endoscope magnetic field based localization system design," in *Proc. IEEE Wireless Commun. Netw. Conf.*, Apr. 2010, pp. 1–6, doi: [10.1109/WCNC.2010.5506718](https://doi.org/10.1109/WCNC.2010.5506718).
- [17] C. Hu, M. Qinghu Meng, and M. Mandal, "Efficient magnetic localization and orientation technique for capsule endoscopy," in *Proc. IEEE/RSJ Int. Conf. Intell. Robots Syst.*, Apr. 2005, pp. 3365–3370, doi: [10.1109/IROS.2005.1545490](https://doi.org/10.1109/IROS.2005.1545490).
- [18] D. Son, S. Yim, and M. Sitti, "A 5-D localization method for a magnetically manipulated untethered robot using a 2-D array of Hall-effect sensors," *IEEE/ASME Trans. Mechatronics*, vol. 21, no. 2, pp. 708–716, Apr. 2016, doi: [10.1109/TMECH.2015.2488361](https://doi.org/10.1109/TMECH.2015.2488361).
- [19] T. Duc Than, G. Alici, S. Harvey, G. O'Keefe, H. Zhou, W. Li, T. Cook, and S. Alam-Fotias, "An effective localization method for robotic endoscopic capsules using multiple positron emission markers," *IEEE Trans. Robot.*, vol. 30, no. 5, pp. 1174–1186, Oct. 2014, doi: [10.1109/TRO.2014.2333111](https://doi.org/10.1109/TRO.2014.2333111).
- [20] N. Marya, A. Karellas, A. Foley, A. Roychowdhury, and D. Cave, "Computerized 3-dimensional localization of a video capsule in the abdominal cavity: Validation by digital radiography," *Gastrointestinal Endoscopy*, vol. 79, no. 4, pp. 669–674, Apr. 2014, doi: [10.1016/j.gie.2013.11.022](https://doi.org/10.1016/j.gie.2013.11.022).
- [21] J. Bulat, "Data processing tasks in wireless GI endoscopy: Image-based capsule localization & navigation and video compression," in *Proc. Conf. IEEE Eng. Med. Biol.*, vol. 3, 2007, pp. 2815–2818, doi: [10.1109/IEMBS.2007.4352914](https://doi.org/10.1109/IEMBS.2007.4352914).
- [22] L. Liu, C. Hu, W. Cai, and M. Q. H. Meng, "Capsule endoscope localization based on computer vision technique," *Proc. IEEE Eng. Med. Biol. Soc. Eng. Futur. Biomed.*, 2009, pp. 3711–3714, doi: [10.1109/IEMBS.2009.5334803](https://doi.org/10.1109/IEMBS.2009.5334803).
- [23] G. Bao, L. Mi, Y. Geng, M. Zhou, and K. Pahlavan, "A video-based speed estimation technique for localizing the wireless capsule endoscope inside gastrointestinal tract," in *Proc. 36th IEEE Eng. Med. Biol. Soc.*, Apr. 2014, pp. 5615–5618, doi: [10.1109/EMBC.2014.6944900](https://doi.org/10.1109/EMBC.2014.6944900).
- [24] A. Karargyris and A. Koulaouzidis, "OdoCapsule: Next-generation wireless capsule endoscopy with accurate lesion localization and video stabilization capabilities," *IEEE Trans. Biomed. Eng.*, vol. 62, no. 1, pp. 352–360, Jan. 2015, doi: [10.1109/TBME.2014.2352493](https://doi.org/10.1109/TBME.2014.2352493).
- [25] G. Bao, K. Pahlavan, and L. Mi, "Hybrid localization of microrobotic endoscopic capsule inside small intestine by data fusion of vision and RF sensors," *IEEE Sensors J.*, vol. 15, no. 5, pp. 2669–2678, May 2015, doi: [10.1109/JSEN.2014.2367495](https://doi.org/10.1109/JSEN.2014.2367495).
- [26] M. Turan, Y. Almalioglu, E. P. Ornek, H. Araujo, M. F. Yanik, and M. Sitti, "Magnetic-visual sensor fusion-based dense 3D reconstruction and localization for endoscopic capsule robots," *Proc. IEEE Int. Conf. Intell. Robot. Syst.*, Oct. 2018, pp. 1283–1289, doi: [10.1109/IROS.2018.8594485](https://doi.org/10.1109/IROS.2018.8594485).

- [27] M. Pourhomayoun, Z. Jin, and M. L. Fowler, "Accurate localization of in-body medical implants based on spatial sparsity," *IEEE Trans. Biomed. Eng.*, vol. 61, no. 2, pp. 590–597, Feb. 2014, doi: [10.1109/TBME.2013.2284271](https://doi.org/10.1109/TBME.2013.2284271).
- [28] Y. Ye, K. Pahlavan, G. Bao, P. Swar, and K. Ghaboosi, "Comparative performance evaluation of RF localization for wireless capsule endoscopy applications," *Int. J. Wireless Inf. Netw.*, vol. 21, no. 3, pp. 208–222, Sep. 2014, doi: [10.1007/s10776-014-0247-7](https://doi.org/10.1007/s10776-014-0247-7).
- [29] A. R. Nafchi, S. T. Goh, and S. A. R. Zekavat, "Circular arrays and inertial measurement unit for DOA/TOA/TDOA-based endoscopy capsule localization: Performance and complexity investigation," *IEEE Sensors J.*, vol. 14, no. 11, pp. 3791–3799, Nov. 2014, doi: [10.1109/JSEN.2014.2331244](https://doi.org/10.1109/JSEN.2014.2331244).
- [30] S. Ting Goh, S. A. Reza Zekavat, and K. Pahlavan, "DOA-based endoscopy capsule localization and orientation estimation via unscented Kalman filter," *IEEE Sensors J.*, vol. 14, no. 11, pp. 3819–3829, Nov. 2014, doi: [10.1109/JSEN.2014.2342720](https://doi.org/10.1109/JSEN.2014.2342720).
- [31] P. Brida and J. Machaj, "A novel enhanced positioning trilateration algorithm implemented for medical implant in-body localization," *Int. J. Antennas Propag.*, vol. 2013, pp. 1–10, Feb. 2013, doi: [10.1155/2013/819695](https://doi.org/10.1155/2013/819695).
- [32] G. Bao, L. Mi, and K. Pahlavan, "A video aided RF localization technique for the wireless capsule endoscope (WCE) inside small intestine," in *Proc. 8th Int. Conf. Body Area Netw.*, 2013, pp. 55–61, doi: [10.4108/icst.bodynets.2013.253642](https://doi.org/10.4108/icst.bodynets.2013.253642).
- [33] C. Hu, Y. Ren, X. You, W. Yang, S. Song, S. Xiang, X. He, Z. Zhang, and M. Q.-H. Meng, "Locating intra-body capsule object by three-magnet sensing system," *IEEE Sensors J.*, vol. 16, no. 13, pp. 5167–5176, Jul. 2016, doi: [10.1109/JSEN.2016.2558198](https://doi.org/10.1109/JSEN.2016.2558198).
- [34] Wikipedia contributors. (2019). *Magnetoquasistatic Field*, *Wikipedia, The Free Encyclopedia*. [Online]. Available: [https://en.wikipedia.org/w/index.php?title=Magnetoquasistatic\\_field&oldid=925317534](https://en.wikipedia.org/w/index.php?title=Magnetoquasistatic_field&oldid=925317534)
- [35] Paperno and A. Plotkin, "3D magnetic tracking of a single subminiature coil with a large 2D-array of uniaxial transmitters," in *Proc. Int. Magn. Conf.*, 2003, pp. 3295–3297, doi: [10.1109/INTMAG.2003.1230365](https://doi.org/10.1109/INTMAG.2003.1230365).
- [36] A. Plotkin, V. Kucher, Y. Horen, and E. Paperno, "A new calibration procedure for magnetic tracking systems," *IEEE Trans. Magn.*, vol. 44, no. 11, pp. 4525–4528, Nov. 2008, doi: [10.1109/TMAG.2008.2003056](https://doi.org/10.1109/TMAG.2008.2003056).
- [37] M. N. Islam and A. J. Fleming, "A novel and compatible sensing coil for a capsule in wireless capsule endoscopy for real time localization," *Proc. IEEE Sensors*, Dec. 2014, pp. 1607–1610, doi: [10.1109/ICSENS.2014.6985326](https://doi.org/10.1109/ICSENS.2014.6985326).
- [38] K. M. Popek, T. Schmid, and J. J. Abbott, "Six-Degree-of-Freedom localization of an untethered magnetic capsule using a single rotating magnetic dipole," *IEEE Robot. Autom. Lett.*, vol. 2, no. 1, pp. 305–312, Jan. 2017, doi: [10.1109/LRA.2016.2608421](https://doi.org/10.1109/LRA.2016.2608421).
- [39] J. J. Craig, *Introduction to Robotics. Mechanics and Control*, 3th ed. London, U.K.: Pearson, 2005.
- [40] J. William H. Hayt, *Engineering Electromagnetics*, 8th ed. New York, NY, USA: McGraw-Hill, 2010.



**SI-LIANG LIU** received the B.S. degree from the School of Mechanical Engineering, Chonnam National University, Gwangju, South Korea, in 2019, where he is currently pursuing the M.S. degree. He is also a Researcher with the Robot Research Initiative (RRI), Chonnam National University. His research interests include microrobot, medical robot, and electromagnetic field.



**JAYOUNG KIM** received the B.S. and M.S. degrees from the Department of Mechanical Engineering, Chungbuk National University, in 2008 and 2011, respectively, and the Ph.D. degree from the Department of Mechatronics Engineering, Chungnam National University, in 2018. He is currently a Senior Researcher with the Korea Institute of Medical Microrobotics and the Robot Research Initiative (RRI), Chonnam National University. His research interests

include AI-based prediction, dynamic mechanisms, and control systems for micro/macro robots.



**BYUNGJEON KANG** received the B.S. and M.S. degrees in mechanical engineering from Chonnam National University, Gwangju, South Korea, in 2008 and 2010, respectively, and the Ph.D. degree in biorobotics from Scuola Superiore Sant'Anna, Pisa, Italy, in 2015.

He is currently a Senior Research Scientist with the Korea Institute of Medical Micro-robotics, Chonnam National University. His research interests include microactuator/robot and micromanipulation for biomedical applications.



**EUNPYO CHOI** received the B.S., M.S., and Ph.D. degrees from the Department of Mechanical Engineering, Sogang University, South Korea, in 2008, 2010, and 2015, respectively. He was a Senior Postdoctoral Fellow with the Department of Bioengineering, University of Washington, USA. He is currently an Assistant Professor with the School of Mechanical Engineering, Chonnam National University, South Korea. His research interests include BioMEMS and micro/nanorobots for medical approaches.



**AYOUNG HONG** (Member, IEEE) received the B.S. and M.S. degrees in mechanical engineering from the Korea Advanced Institute of Science and Technology, Daejeon, South Korea, in 2009 and 2012, respectively, and the Ph.D. degree from the Department of Mechanical and Process Engineering, ETH Zurich, Zurich, Switzerland, in 2019. She is currently an Assistant Professor in robotics engineering with the College of AI Convergence, Chonnam National University, South Korea. Her

main research interest includes the design and control of soft robots in the biomedical applications.



**JONG-OH PARK** (Member, IEEE) received the B.S. and M.S. degrees from the Department of Mechanical Engineering, South Korea, in 1978 and 1981, respectively, and the Ph.D. degree in robotics from Stuttgart University, Germany, in 1987. From 1982 to 1987, he was a Guest Researcher at the Fraunhofer-Institut für Produktionstechnik und Automatisierung (FhG IPA), Germany. He was a Principal Researcher at the Korea Institute of Science and Technology

(KIST), from 1987 to 2005, where he was the Director of the Microsystem Research Center, from 1999 to 2005. In 2005, he moved to Chonnam National University, where he is currently a Full Professor with the School of Mechanical Engineering and the Director of the Robot Research Initiative (RRI). His research interests include biomedical microrobots, medical robots, and service robots.



**CHANG-SEI KIM** (Member, IEEE) received the B.S. degree from the Department of Control and Mechanical Engineering, Pusan National University, in 1998, the M.S. degree from the Department of Mechanical Design and Production Engineering, Seoul National University, in 2000, and the Ph.D. degree from the School of Mechanical Engineering, Pusan National University, in 2011. He was a Research Associate with the Department of Mechanical Engineering, University of Maryland at College Park, USA. He is currently an Assistant Professor with the School of Mechanical Engineering, Chonnam National University, South Korea. His research interests include dynamics and control applications for mechanical and biomedical systems in the real world.